

Detection of Extended Hot Water in the Outflow from NGC 2071

Gary J. Melnick, Volker Tolls

Harvard-Smithsonian Center for Astrophysics, 60 Garden Street, Cambridge, MA 02138

gmelnick@cfa.harvard.edu, vtolls@cfa.harvard.edu

David A. Neufeld, Yuan Yuan, Paule Sonnentrucker

*Department of Physics and Astronomy, Johns Hopkins University, 3400 North Charles Street,
Baltimore, MD 21218*

neufeld@pha.jhu.edu, yuanyuan@pha.jhu.edu, sonnentr@pha.jhu.edu

Dan M. Watson

Department of Physics and Astronomy, University of Rochester, Rochester, NY 14627

dmw@pas.rochester.edu

Edwin A. Bergin

*Department of Astronomy, University of Michigan, 825 Dennison Building, Ann Arbor, MI
48109*

ebergin@umich.edu

and

Michael J. Kaufman

*Department of Physics and Astronomy, San Jose State University, One Washington Square,
San Jose, CA 95192-0106*

mkaufman@email.sjsu.edu

ABSTRACT

We report the results of spectroscopic mapping observations carried out toward a $\sim 1' \times 1'$ region within the northern lobe of the outflow from NGC 2071 using the Infrared Spectrograph (IRS) of the *Spitzer Space Telescope*. These observations covered the 5.2–37 μm spectral region and have led to the detection of a number of ionic, atomic, and molecular lines, including fine-structure emission of Si^+ , Fe^+ , S^{++} , S, the S(0)-S(7) pure rotational lines of H_2 , the R(3) and R(4) transitions of HD, and at least 11 transitions of H_2O . In addition, the 6.2, 7.4, 7.6, 7.9, 8.6 and 11.3 μm PAH emission bands were also observed and several transitions of OH were tentatively detected. Most of the detected line transitions were strong enough to map including, for the first time, three transitions of hot H_2O . We find that: (1) the water emission is extended; (2) the extended emission is aligned with the outflow; and, (3) the spatial distribution of the water emission generally follows that observed for H_2 . The *Spitzer*/IRS data suggest that both dissociative and non-dissociative shocks are present in the portion of the outflow observed here. Most of H_2 , H_2O S(2)-S(7), HD, and S I emission detected likely arises from behind the non-dissociative shock, while the Si II, Fe II, and most of the H_2 S(1) emission originate from behind the dissociative shock. Based on the measured line intensities, we derive an HD abundance relative to H_2 of $1.1\text{--}1.8 \times 10^{-5}$ and an H_2O number density of $12\text{--}29\text{ cm}^{-3}$. The H_2 density in the water-emitting region is not well constrained by our observations, but is likely between 3×10^4 and 10^6 cm^{-3} , yielding an H_2O abundance relative to H_2 of between 2×10^{-5} and 6×10^{-4} . Future observations planned for the *Herschel Space Observatory* should greatly improve the density estimate, and thus our knowledge of the H_2O abundance, for the water-emitting regions reported here. Finally, we note a possible departure from the H_2O ortho-to-para ratio of 3:1 expected for water formed in hot post-shocked gas, suggesting that a significant fraction of the water vapor we detect may arise from H_2O sputtered from cold dust grains.

Subject headings: ISM: Abundances, ISM: Jets and Outflows, ISM: Molecules, Stars: Formation, Stars: Winds, Outflows

1. Introduction

Outflows from young stellar objects provide a natural laboratory toward which it is possible to test the predictions of chemical models thought to apply to warm ($T \gtrsim 300\text{K}$), dense ($n(\text{H}_2) \gtrsim 10^4 \text{ cm}^{-3}$) gas. Among these predictions is that water will be formed rapidly in the warm gas via a set of neutral-neutral reactions (cf. Elitzur & de Jong 1978; Elitzur & Watson 1978). Moreover, these reactions can potentially convert all of the oxygen not locked in CO into H_2O (cf. Bergin, Melnick, & Neufeld 1998). Indeed, the gas-phase water abundances toward shock-heated gas associated with outflows is found to be higher than that within cold, quiescent molecular clouds (cf. Harwit *et al.* 1998; Melnick *et al.* 2000; Neufeld *et al.* 2000; Nisini *et al.* 2000; Benedettini *et al.* 2002), although the inferred abundances rarely approach $[\text{H}_2\text{O}]/[\text{H}_2] \sim 10^{-4}$ as would be expected for the full conversion of all oxygen not in CO into H_2O . In addition, an unknown fraction of the elevated gas-phase water abundance is likely due to the removal of water-ice from grains that pass through nondissociative shocks (Draine, Roberge, & Dalgarno 1983). Based on a detailed analysis of ground-state ortho-water spectra obtained by the *Submillimeter Wave Astronomy Satellite* (SWAS) toward 18 outflow sources, Franklin *et al.* (2008) propose that the lower-than-expected water abundances within these sources is due to the small fraction of outflow material that actually passes through strong shocks. This also implies that the beam filling factor of regions with highly-abundant water is lower than previously assumed.

Unfortunately, these previous observations lacked the spatial resolution to determine the detailed water distribution. Thus, the interpretation was hampered by uncertainties in both the fraction of the beam filled with H_2O emission and the physical conditions in the H_2O -emitting gas as might be revealed by co-spatial emission from H_2 . With beam sizes that range between $1.8''$ and $5.5''$, depending on wavelength, and high sensitivity, the Infrared Spectrometer (IRS) aboard the *Spitzer Space Telescope* has enabled the study of H_2O , H_2 , and HD with unprecedented detail. In this paper, we describe observations of the outflow source NGC 2071 and report the first detection of spatially extended, hot H_2O vapor with *Spitzer*/IRS. In addition to H_2O , we have also mapped the ground-vibrational state distribution of H_2 , as well as low-lying rotational and fine-structure emission from HD, S I, Fe II, and Si II.

NGC 2071 is a region of active star formation, located inside the northern part of the Orion B (L 1630) molecular cloud complex at a distance of 390 pc (Anthony-Twarog 1982). The region of interest in this study lies approximately $4'$ north of the optical reflection nebula NGC 2071 and is the site of a prominent outflow. Fig. 1 shows a portion of the outflow, as delineated by the H_2 1-0 S(1) $2.12\mu\text{m}$ emission (Eisloffel 2000), along with the region observed

here. Near-infrared continuum imaging and spectroscopy of this area reveal a cluster of infrared sources near the center of this outflow (Walther *et al.* 1991, 1993). The detection of a bipolar thermal radio jet from source IRS3 oriented in the direction of the NGC 2071 North flow, and of a ring of H₂O maser spots perpendicular to the flow axis (Torrelles *et al.* 1998), suggest that IRS3 is the driving source of the NGC 2071 North flow. The outflow, which extends more than 6', has been mapped previously in CO (Snell *et al.* 1984; Moriarty-Schieven, Hughes & Snell 1989), CS (Zhou *et al.* 1991), SO, SiO, and HCO⁺ (e.g., Chernin & Masson 1992, 1993), and in H₂ 1-0 S(1) (e.g., Eisloffel 2000, and references therein). The presence of high-velocity gas – as high as 60 km s⁻¹ – and the enhanced abundance of species such as SO and SiO (e.g., Chernin & Masson 1993) suggest that shock processing of the outflow gas is highly likely.

In this paper, we present the results of *Spitzer*/IRS observations toward the northern lobe of the NGC 2071 outflow and discuss the new understanding revealed through high spatial resolution mapping in the lines of H₂ S(0)–S(7), HD R(3) and R(4), Si II, Fe II, S I, and three transitions of H₂¹⁶O: 7₂₅–6₁₆, 6₃₄–5₀₅, and 7₃₄–6₂₅. In addition, we present spectra that include several other H₂O features along with several lines that we tentatively ascribe to OH. Section 2 summarizes the observations and Section 3 presents the results. Section 4 describes the calculations used to analyze the line data and the conclusions are discussed in Section 5.

2. Observations and Data Reduction

NGC 2071 was observed on 20 and 21 October 2004 as part of *Spitzer Space Telescope* Cycle 1 General Observer (GO) program 3423. The observations utilized the Long-High (LH), Short-High (SH), and Short-Low (SL) modules to achieve the highest possible spectral resolving power and complete spectral coverage available to IRS. The mapped areas were approximately 1' × 1' for LH and SH and approximately 1' × 1.5' for SL, obtained by stepping in spacings of half-slit width perpendicular to the slit and in ~4/5 of the slit length parallel to the slit. The raw data were processed with the *Spitzer* Science Center (SSC) pipeline version S12.0.2, which provided basic calibrated data (BCD). Further data reduction utilized a data pipeline developed by our group. This pipeline incorporates procedures for removing bad or “hot” pixels, utilizes the SMART software package (Higdon *et al.* 2004) for calibration and extraction of spectra at each position along the slit, applies a slit loss correction function (SLCF) to correct the flux calibration performed for point-like sources to extended sources, and automatically fits Gaussian lines and second-order polynomials to a set of predetermined spectral lines at each position. The first three steps of this data processing are described in more de-

tail in (Neufeld *et al.* 2006a). The line fitting was performed iteratively to achieve the best-fit parameters. In some cases, the resulting line maps exhibited noticeable striping attributable to varying pixel sensitivity across the slit and by the after-effects of correcting for bad pixels. A pixel response correction factor (PRCF) was determined to remove striping in the final maps of all LH and SH observations. We used a statistical approach to determine the relative sensitivity in each pixel while preserving the total flux in all pixels across the slit. Details of this method are provided in Neufeld *et al.* (2007).

3. Results

The observed spectra show emission from molecular, atomic and ionic species as well as a number of PAH features. In particular, we detect emission from [S I], [S III], [Fe II] and [Si II] transitions, H₂ rotational lines from S(0) to S(7), HD R(3) and R(4) transitions, and at least 11 H₂O transitions. Most of the line emission was strong enough to detect over extended regions and these maps are shown in Figs. 2 - 6. All maps have been normalized to the peak line intensities listed in Table 1. For reference, the positions of the three strongest peaks in the H₂ S(1) 17 μ m emission are marked as P1, P2, and P3 on these maps. As can be seen in Fig. 4, the strongest water emission lies close to the peak of the H₂ S(1) 17 μ m emission (position P1 in Fig. 4). It is also clear that: (1) the water emission is extended; (2) this extended emission is generally aligned with the outflow; and, (3) the water emission exhibits secondary peaks toward positions of enhanced H₂ emission. Fig. 7 shows a direct comparison of the spatial distribution of the H₂O (7₂₅ – 6₁₆) emission versus that due to the ro-vibrational H₂ 1-0 S(1) and pure rotational H₂ S(1) emission. While the overall distribution of the two species is quite similar, the peaks of the H₂O and H₂ are sometimes offset with respect to each other. For example, the peaks of the H₂O 7₂₅ – 6₁₆ and the H₂ S(1) emission are offset by 3.8'', which exceeds the stated IRS sky registration error, and thus is likely real.

The spectra obtained toward the water emission peaks closest to positions P1 and P2 are shown in Figs. 8 – 10. In order to reduce the baseline noise, we averaged the data toward the water peaks using a Gaussian weighing function with a wavelength-dependent HPBW of between 11.0'' at 27.0 μ m and 14.7'' at 5.5 μ m. The final synthetic beams have effective beam widths of 15'' for all wavelengths of interest (cf. Neufeld *et al.* 2006a). The spectrum labeled H₂O Peak 1 is centered at RA 05^h 47^m 04^s.6, Dec +00° 22' 52.2'' (J2000), while the spectrum labeled H₂O Peak 2 is centered at RA 05^h 46^m 40^s.4, Dec +00° 22' 43.0'' (J2000). For almost all of the H₂O and H₂ transitions detected, the 15'' synthetic beam is sufficiently large to encompass

the water emission as well as the bulk of the H_2 emission toward each peak. The measured line fluxes for the water features associated with H_2O Peak 1 are provided in Table 2. Unfortunately, at the spectral resolving power of the *Spitzer*/IRS, many of the H_2O features are blends of two or more H_2O transitions. The extinction-corrected line fluxes for the other key species in this spectrum are given in Table 3. We also note the tentative detection of emission from a number of OH rotational transitions (see Figs. 8 and 9) whose upper levels lie as much as ~ 3500 K above the ground.

Direct measures of the extinction toward the NGC 2071 outflow are not available. Instead, we inferred the required extinction corrections as a function of wavelength in the *Spitzer* bandpass by fitting the wings of the silicate absorption feature at $9.7\ \mu\text{m}$, hence minimizing the effects of line saturation when present. Our silicate fitting model uses the renormalized synthetic Galactic extinction curve per unit hydrogen column density calculated for $R_V = 3.1$ or for $R_V = 5.5$ (Draine 2003a,b) in linear combination with a first-degree polynomial and 4 Gaussians with fixed widths and fixed centers to account for emission from interfering lines. Since the gas clumps probed by our data have dust properties most probably intermediate between diffuse and dense molecular clouds, the extinction corrections we adopted represent the mean of the extinction corrections we obtained for $R_V = 3.1$ and those we obtained for $R_V = 5.5$.

4. Water Calculations

To assess how the H_2O line strengths measured here constrain the water abundance, the equilibrium level populations of all ortho and para rotational levels of the ground H_2^{16}O vibrational state with energies E/k up to 7700 K have been calculated using an escape probability method described by Neufeld & Melnick (1991). In modeling the excitation of water vapor, we are limited by the availability of molecular data. Thus far, at the high temperatures of relevance here, a complete set of rate coefficients has only been computed for collisional excitation of H_2O by He (Green, Maluendes & McLean 1993). A new and accurate nine-dimensional potential energy surface has recently been computed for $\text{H}_2\text{O}-\text{H}_2$ (Faure *et al.* 2005), and quantal calculations are currently underway (Dubernet 2007, personal communication), to obtain rate coefficients for the collisional excitation of H_2O by H_2 . However, quantal results for transitions involving the highly-lying rotational states observed by *Spitzer* have not yet been completed. Nevertheless, for the subset of those transitions that show the largest rate coefficients, Faure *et al.* (2007) have recently performed quasi-classical trajectory (QCT) calculations to estimate the collisional rates, and have kindly made the results available to us prior to publication.

Unfortunately, transitions with small rate coefficients still play a significant role in the excitation of the spectral lines that we have observed with *Spitzer*; for those transitions, we have had to use the Green, Maluendes & McLean (1993) results, scaled by a factor 1.348 to account for the difference between the H₂O-He and H₂O-H₂ reduced masses. Finally, a polynomial fit to the exact expression for the photon escape probability from a plane-parallel emitting region (Hummer & Rybicki 1982) is used.

We assume that the physical conditions within H₂O Peak 1 are those required to reproduce the measured H₂ S(0) through S(7) flux from the same region. Table 4 summarizes these physical conditions. The model H₂ column densities are assumed to be those consistent with a simple shock model in which

$$N(H_2) = 6.45 \times 10^{20} \left[\frac{n(H_2)}{10^5} \right]^{0.5} \left[\frac{T_{gas}}{1000} \right]^{-0.555} \text{ cm}^{-2}, \quad (1)$$

where $n(H_2)$ is the density in the postshock gas (cf. Neufeld *et al.* 2006a). We assume that the fraction of the beam filled by the warm and hot H₂O is given by the ratio of the measured values of $N(H_2)$ given in Table 4 to those derived above. To estimate the physical parameters from the eight H₂ rotational lines, we have performed calculations in which the emitting region is approximated by a two-component model for two different cases: (1) clouds with homogenous density; and, (2) clouds with homogenous pressure. The six best-fit parameters (temperature, column density and H₂ ortho-to-para ratio for the two components) are determined by minimizing the root mean square of $\ln(\text{measured flux}/\text{computed flux})$ for the H₂ S(0) to S(7) lines. Results were obtained for a series of H₂ number densities ranging from 10^4 to 10^7 cm^{-3} , and pressures ($\times 1/k$) ranging from 10^7 to $10^{10} \text{ cm}^{-3} \text{ K}$. The greatest differences between the two models – homogenous density or pressure – appear at low densities (or low pressures), where the pressure-balanced assumption requires a relatively higher temperature for the hot component. The results of the two models converge as LTE is approached for the higher-lying transitions, i.e., for number densities greater than 10^5 cm^{-3} (or pressures/ k greater than $10^8 \text{ cm}^{-3} \text{ K}$). In this case, the best-fit temperature for the warm component is around 300-360 K while that for the hot component is around 1000-1500 K.

Using the physical conditions that best fit the H₂ observations, the abundances of H₂O and HD toward H₂O Peak 1 were then derived. For H₂O, the total (ortho+para) abundance at each assumed density was varied to produce the best overall fit to the features listed in Table 2. We choose these features to fit because they are the strongest observed transitions between 5 and $36.5 \mu\text{m}$ toward H₂O Peak 1; both the observed and predicted line fluxes for H₂O transitions

lying at $\lambda < 29 \mu\text{m}$ are less than 5 MJy/sr, and most typically less than about 3 MJy/sr, rendering their unambiguous identification above the noise difficult. As discussed further below, the H_2O ortho-to-para ratio was treated as a free parameter. Similarly, the abundance of HD was determined by fitting the measured R(3) and R(4) line fluxes, although the best-fit HD abundance is not a sensitive function of number density due to the moderately low critical densities of the R(3) and R(4) transitions of $\sim 10^4$ to 10^5 cm^{-3} . Finally, it would be useful to also fit the measured OH rotational lines. Unfortunately, the lack of reliable collisional rate coefficients for these high-lying transitions makes the results of such a calculation uncertain at this time.

As shown in Fig. 11, fits to the H_2 and HD emission lines alone favor gas with higher densities or pressures. The best-fit HD abundance relative to H_2 is between 1.1×10^{-5} and 1.8×10^{-5} , with only a weak dependence on density as noted above. This abundance is very similar to those derived previously from observations of HD R(3) and R(4) in other shocked regions that we have observed with *Spitzer* (Neufeld *et al.* 2006b). Fits to the H_2O features were computed in two ways. First, fits to ten of the eleven H_2O features in Table 2 were calculated assuming an H_2O ortho-to-para ratio of 3:1 as well as an ortho-to-para ratio that was allowed to vary in order to achieve the best overall fit at each density between 10^4 and 10^7 cm^{-3} . The strong feature at $34.55 \mu\text{m}$ was not included. The conditions needed to reproduce the flux in this line resulted in fluxes in the other H_2O transitions that are in significant disagreement with the observations. Thus, we conclude that either this line is blended with an unknown feature or uncertainties in the collision rates may be resulting in lower-than-actual populations in the upper 7_{34} state. Second, to better isolate the effects of varying the H_2O ortho-to-para ratio, we examined the three strongest features in which the only contribution to the line flux was an ortho- H_2O transition, at $29.84 \mu\text{m}$, or a para- H_2O transition, at 33.13 and $36.21 \mu\text{m}$. These results are also shown in Fig. 11. Based on fits to the water data alone, H_2 densities in the water-emitting region of between about 3×10^4 and $3 \times 10^5 \text{ cm}^{-3}$ appear favored. The best fits to the isolated ortho and para features are achieved for H_2 densities between 3×10^4 and 10^5 cm^{-3} and an assumed H_2O ortho-to-para ratio of between 1.5 and 1.6.

The best-fit water abundances are shown in Fig. 12. To a good approximation, the best fits to the H_2O line fluxes are proportional to the H_2 density \times the water abundance, resulting in a derived number density of H_2O molecules of $12 - 29 \text{ cm}^{-3}$, independent of H_2 density. This is a consequence of the fact that the observed transitions have critical densities $> 10^9 \text{ cm}^{-3}$ and are optically thin under the conditions considered here. In this limit, the flux in an ortho- H_2O (or para- H_2O) line is

$$F = \frac{A_{ul} h\nu_{ul} N_u \Omega}{4\pi} = \frac{A_{ul} h\nu_{ul} [n(\text{H}_2) \cdot \ell \cdot \chi(\text{H}_2\text{O}) \cdot f_u \cdot \xi_{\text{op}}] \Omega}{4\pi}, \quad (2)$$

where A_{ul} is the transition spontaneous emission rate, ν_{ul} is the transition frequency, $n(\text{H}_2)$ is the H_2 density, ℓ is the depth of the emitting region, $\chi(\text{H}_2\text{O})$ is the water abundance relative to H_2 , f_u is the fractional population in the upper state of the emitting transition, ξ_{op} is the fraction of all H_2O molecules in the ortho (or para) state, and Ω is the solid angle of the water emitting region.

Fig. 13 shows the resulting 29 – 36.5 μm water spectrum computed for an H_2 density of 10^5 cm^{-3} and H_2O ortho-to-para ratios of 3:1 and 1.55:1, the latter being the best-fit ortho-to-para ratio at a density of 10^5 cm^{-3} . The computed spectra were convolved with a Gaussian profile whose width was selected to match the IRS Long-High resolving power, $\lambda/\Delta\lambda$, of 600 (FWHM). As can be seen in Fig. 13, the differences between the spectrum computed assuming an H_2O ortho-to-para ratio of 3:1 and 1.55:1 are small. Nevertheless, assuming an ortho-to-para ratio less than 3:1 results in a slightly better overall fit to the H_2O data and suggests a possible departure from the usual assumption that water in post-shocked gas is always present in the LTE ortho-to-para ratio of 3:1. This tentative finding is discussed further in the next section.

Taking into account the H_2 , HD, and H_2O spectra, the overall best fits to these data favor an H_2 density in the range 3×10^4 to 10^6 cm^{-3} , and $2 \times 10^{-5} \lesssim \chi(\text{H}_2\text{O}) \lesssim 6 \times 10^{-4}$. Unfortunately, the present data do not allow us to better constrain the H_2 density, and thus the water abundance, within the emitting region. However, as we discuss in the next section, future observations planned for the *Herschel Space Observatory* may permit more direct measures of the H_2 density.

5. Discussion

The capabilities of the *Spitzer*/IRS instrument has enabled the study of outflow regions in ways not possible previously. In particular, the ability to map the distribution and intensity of key species, like H_2 , HD, Fe^+ , Si^+ , S, and, of course, H_2O , with a spatial resolution of a few arcseconds permits more stringent tests of our understanding of the structure and composition of outflows. Earlier space missions, such as the *Infrared Space Observatory* (ISO), *SWAS*, and *Odin* have established the correlation between outflows from young stellar objects and strong water emission (e.g., Harwit *et al.* 1998; Melnick *et al.* 2000; Neufeld *et al.* 2000; Nisini *et al.* 2000; Giannini, Nisini, & Lorenzetti 2001; Benedettini *et al.* 2002). Unfortunately, these observations were conducted with large beams relative to *Spitzer*/IRS or, in the case of

the *ISO* Short-Wavelength Spectrometer with its $10''$ beam, lower sensitivity than *Spitzer*/IRS. As a result, the filling factor of H_2O within the beam was not always directly known or key species helpful in the interpretation of the water data, like H_2 and HD, were not detected. The observations reported here remedy most, but not all, of these previous shortcomings.

The primary goal of this study is the further understanding of water in outflows. Unlike the production of water in quiescent molecular clouds, which proceeds via a set of relatively slow ion-neutral reactions in the gas phase (e.g., Herbst, E., & Klemperer 1973), or through the photodesorption of water formed on the surface of dust grains (e.g., Hollenbach *et al.* 2008), the material in outflows often passes through a shock which both compresses and heats the gas. In the post-shocked region of non-dissociative, or *C*-type, shocks (Draine 1980), with shock velocities, $v_s, \gtrsim 10 \text{ km s}^{-1}$, temperatures exceed 300 K enabling a pair of neutral-neutral reactions ($\text{H}_2 + \text{O} \rightarrow \text{OH} + \text{H}$ and $\text{H}_2 + \text{OH} \rightarrow \text{H}_2\text{O} + \text{H}$) that can rapidly convert all gas-phase oxygen not bound in CO into H_2O (Elitzur & de Jong 1978). For $v_s \gtrsim 50 \text{ km s}^{-1}$, most *C*-type shocks break down, giving rise to dissociative, or *J*-type, shocks. Molecules are completely dissociated, either by the precursor UV field generated by the hot gas near the shock front or by collisions in the shock, and then reform on grain surfaces in the cooler ($\sim 400 \text{ K}$) downstream gas (Hollenbach & McKee 1989). Because *C*-type shocks have very low ionic abundances, strong Si II ($34.8 \mu\text{m}$) and Fe II ($26.0 \mu\text{m}$) emission is considered a tracer of *J*-type shocks.

The *Spitzer*/IRS data suggest that both *J*- and *C*-type shocks are present in the portion of the outflow observed here. The strong Si II and Fe II emission evident in Fig. 6 follows the outflow, peaking close to H_2 positions P3 and P2, and lies closer to the source of the outflow than the most prominent H_2 position, P1. This may indicate the presence of fast-moving gas along the center of the outflow which has been slowed as it approaches position P1. This picture is supported by previous CO $J = 3-2$ observations (Chernin & Masson 1992), which revealed well collimated, high velocity ($30 - 60 \text{ km s}^{-1}$) gas in a symmetric bipolar outflow only within $1.5'$ of the source, presumed close to IRS3. Moreover, the CO data show velocity peaks appearing at $\pm 1'$ from the source. Further support is provided by the pronounced peak in the S I ($25.2 \mu\text{m}$) emission (see Fig. 6) near position P1. In the *J*-type shock models of Hollenbach & McKee (1989), for densities between 10^4 and 10^6 cm^{-3} , the strongest S I emission arises at the lowest velocities (i.e., $v_s \sim 30 \text{ km s}^{-1}$), whereas both the Si II and Fe II emission increase with shock velocity. In addition, previous *Spitzer*/IRS observations of supernovae remnants (Neufeld *et al.* 2007) show a strong correlation between the S I and H_2 S(1)–S(7) spatial distribution, suggesting that most of the S I emission arises in the slower, nondissociative shocks. This could account for the difference in the spatial distribution of Si II, Fe II, and S I.

That the H_2 S(1) peak emission appears to be located closer to the source of the outflow (near IRS 3) than all of the higher-lying H_2 transitions, i.e. S(2) through S(7), as well as that of the H_2O may also be explained by this scenario. In the multiple shock picture, the H_2 S(1) emission could arise primarily in the ~ 400 K gas behind a moderate J -type shock – the post shock region in which it is predicted that H_2 is reformed (Hollenbach & McKee 1989). Meanwhile, the higher-lying H_2 and H_2O lines would arise from behind the C -type shock slightly farther from the outflow source in which gas temperatures can heat molecules to more than 2000 K.

The good fit to the H_2 and HD data (see Fig. 11) obtained with conditions characteristic of a C -type shock provide the best evidence for the coexistence of a non-dissociative shock. Based on the morphology of the Si II, Fe II, and H_2 emission, it is tempting to suggest that the C -type shock emission arises in the entrained slower moving shocked material surrounding the high-velocity J -type shock gas which, itself, slows and transitions to a C -type shock near position P1.

That the water emission follows closely the H_2 emission is in accord with the predictions of C -type shock models. Unfortunately, our inability to unambiguously determine the H_2 density in the water-emitting region from the *Spitzer*/IRS data prevents us from fully testing the other key prediction of the C -type shock models – namely that the water abundance will be high (i.e., $\chi(\text{H}_2\text{O}) \gtrsim 10^{-4}$) in the post-shocked gas. Other observations provide general support for the density range preferred here. Zhou *et al.* (1991) have observed the NGC 2071 outflow in the CS $J = 2-1$, 5-4, 6-5, and 7-6 transitions. Their best fit to the CS wing emission yield densities of $1 - 4 \times 10^5 \text{ cm}^{-3}$. Unfortunately, the varying beam sizes with which these observations were conducted, ranging between $11''$ and $24''$, along with uncertainties in the gas temperature and the surface filling factors for the different transitions contribute to the overall uncertainty in the density determination. Nonetheless, if this range of densities applies to H_2O Peak 1 region, then the best-fit water abundance would lie between approximately 5×10^{-5} and 2×10^{-4} relative to H_2 which still represents a significant abundance enhancement above that found in quiescent molecular clouds (e.g., Snell *et al.* 2000) and is consistent with the predictions of C -type shock models.

Future observations of far-IR high- J CO lines – planned for the Photodetector Array Camera and Spectrometer (PACS) instrument aboard the *Herschel Space Observatory* – promise to yield a valuable means of estimating the H_2 density in NGC 2071. Given the gas temperatures and column densities derived from our *Spitzer* observations of the H_2 S(0)–S(7) rotational transitions, we have computed the CO line intensities expected for a CO abundance of 10^{-4} relative to H_2 . The sample results shown in Fig. 14 were obtained by means of a statistical equilibrium

calculation in which we adopted the molecular data described in Neufeld & Kaufman (1993). Fig. 14 indicates that far-IR transitions of CO should be readily detectable with *Herschel* and that their strengths will provide a key probe of the gas density over exactly the desired range: $4 < \log_{10}(\text{H}_2/\text{cm}^{-3}) < 6.5$. Here, the dashed line corresponds to the *Herschel*/PACS spectral line sensitivity of $\sim 2 \times 10^{-6} \text{ erg cm}^{-2} \text{ s}^{-1} \text{ sr}^{-1}$ (5σ in 1 hour, corresponding to a flux of $5 \times 10^{-18} \text{ W m}^{-2}$ into a $9.7 \times 9.7''$ pixel). Because the CO lines are optically-thin, the predicted line intensities are proportional to the assumed CO abundance. However, the far-IR line ratios (Fig. 15) are independent of the assumed CO abundances and would provide a good estimate of densities in the range $5 < \log_{10}(\text{H}_2/\text{cm}^{-3}) < 6.5$ without any required knowledge of the CO abundance.

The question of the distribution and abundance of the gas-phase water is important not only as the answers test the validity of long-standing chemical predictions. Many models of the larger ambient clouds take as a starting point certain molecular enrichment due to the passage of nearby shocks. A recent analysis of 18 molecular outflows by Franklin *et al.* (2008) based on observations of the ground-state ortho- H_2O transition from *SWAS* and the $J = 1-0$ transition of ^{12}CO and ^{13}CO obtained with the Five College Radio Astronomy Observatory shows that the ortho- H_2O abundance (relative to H_2) in most outflows is between 10^{-7} and 10^{-6} , assuming the H_2O and CO emission arises in the same gas. However, an examination of the water abundance as a function of outflow velocity reveals a strong dependence; the water abundance rises with outflow velocity, reaching abundances of $\sim 10^{-4}$ at the highest velocities. However, the mass associated with the highest velocity emission is found to be small compared with the total outflow mass, leading to the conclusion that only a small fraction of the outflowing molecular gas has passed through shocks strong enough to fully convert the gas-phase oxygen to water. Using the measurements obtained here, combined with the data soon to be available from *Herschel*, it will be possible to independently test this conclusion.

Finally, our potential detection of an H_2O ortho-to-para ratio that is not in equilibrium at the gas temperature may hint at the origin of the water vapor emission we detect. The lowest energy level of para- H_2O is $\sim 34 \text{ K}$ below that of ortho- H_2O and, as such, the ratio of the ortho and para populations in LTE is temperature dependent. When water forms in the gas phase via exothermic reactions the energy released is much greater than this energy difference and the ortho-to-para ratio will reflect the 3:1 ratio of statistical weights between these species. When water forms on the surfaces of cold dust grains, it is believed that the energy generated by the chemical reaction is shared with the grain and the water molecules should equilibrate to an ortho-to-para ratio that reflects the grain temperature (e.g., Limbach *et al.* 2006). If the grain temperature is below $\sim 50 \text{ K}$, then the ortho-to-para ratio will lie below 3:1. In this regard, it has

been known for many years that water in numerous cometary comae exhibits an ortho-to-para ratio below 3:1, which has been attributed to formation at temperatures of $\sim 25\text{--}30$ K (e.g., Mumma, Weaver & Larson 1987; Bonev *et al.* 2007).

Our measurements, while uncertain, potentially limit the ortho-to-para ratio to between 1.5–2.5, or equivalent temperatures of $\sim 20\text{--}30$ K. If the water is produced entirely in shocks via the well known sequence of neutral-neutral reactions, the ortho-to-para ratio should be 3:1. However, if the water enters the gas phase via sputtering from cold grain surfaces, then the ratio would reflect equilibrium at the grain temperature. A mixture of both sputtering and gas-phase formation cannot be ruled out and thus this measurement represents an upper limit to the ortho-to-para ratio of water ice. If our measurement is confirmed, this would therefore suggest that a significant amount of the H_2O emission we detect has its source in water vapor produced from grain sputtering and not via gas-phase reactions.

Acknowledgements: G.J.M. gratefully acknowledges the financial support of NASA grant NNG06GB30G from the Long Term Space Astrophysics (LTSA) Research Program and through an award issued by JPL/Caltech (Support Agreement no. 1265773). This work is based on observations made with the *Spitzer Space Telescope*, which is operated by JPL/Caltech under NASA contract 1407.

REFERENCES

- Anthony-Twarog, B.F. 1982, *AJ*, **87**, 1213.
- Benedettini, M., Viti, S., Giannini, T., Nisini, B., Goldsmith, P.F., & Saraceno, P. 2002, *A&A*, **395**, 657.
- Bergin, E.A., Melnick, G.J., & Neufeld, D.A. 1998, *ApJ*, **499**, 777.
- Bonev, B.P., Mumma, M.J., Villanueva, G.L., Disanti, M.A., Ellis, R.S., Magee-Sauer, K., & Dello Russo, N. 2007, *ApJ*, **661**, L97.
- Chernin L.M., & Masson C.R. 1992, *ApJ*, **396**, L35.
- Chernin L.M., & Masson C.R. 1993, *ApJ*, **403**, L21.
- Draine, B. T. 1980, *ApJ*, **241**, 1021.
- Draine, B. T., Roberge, W.G., & Dalgarno, A. 1983, *ApJ*, **264**, 485.
- Draine, B. T. 2003a, *Ann. Rev. Astron. & Astrophys.*, **41**, 214.
- Draine, B. T. 2003b, *ApJ*, **598**, 1017.
- Dubernet, M-L. 2007, personal communication.
- Eisloffel, J. 2000, *A&A*, **354**, 236.
- Elitzur, M., & de Jong, T. 1978, *A&A*, **67**, 323.
- Elitzur, M., & Watson, W.D. 1978, *A&A*, **70**, 443.
- Faure, A., Crimier, N., Ceccarelli, C., Valiron, P., Wiesenfeld, L., & Dubernet, M.L. 2007, *A&A*, **472**, 1029.
- Faure, A., Valiron, P., Wernli, M., Wiesenfeld, L., Rist, C., Noga, J., & Tennyson, J. 2005, *J. Chem. Phys.*, **122**, 1102.
- Franklin, J., Snell, R.L., Kaufman, M.J., Melnick, G.J., Neufeld, D.A., Hollenbach, D.J., & Bergin, E.A. 2008, *ApJ*, **674**, 1015.
- Giannini, T., Nisini, B., & Lorenzetti, D. 2001, *ApJ*, **555**, 40.

- Green, S., Maluendes, S., & McLean, A.D. 1993, ApJS, **85**, 181.
- Harwit, M., Neufeld, D.A., Melnick, G.J., & Kaufman, M.J. 1998, ApJ, **497**, L105.
- Herbst, E., & Klemperer, W. 1973, ApJ, **185**, 505.
- Higdon, S.J.U., Devost, D., Higdon, J. L., Brandl, B. R., Houck, J. R., Hall, P., Barry, D., Charmandaris, V., Smith, J. D. T., Sloan, G. C., & Green, J. 2004, PASP, **116**, 975.
- Hollenbach, D.J., Kaufman, M.J., Bergin, E.A., & Melnick, G.J. 2008, in preparation.
- Hollenbach, D., & McKee, C.F. 1989, ApJ, **342**, 306.
- Hummer, D.G., & Rybicki, G. 1982, ApJ, **254**, 767.
- Limbach, H.J., Buntkowsky, G., Matthes, J., Gründemann, S., Pery, T., Walaszek, B., & Chaudret, B. 2006, Chem. Phys. Chem, **7**, 551.
- Melnick, G.J., Ashby, M.L.N., Plume, R., Bergin, E.A., Neufeld, D.A., Chin, G., Erickson, N.R., Goldsmith, P.F., Harwit, M., Howe, J.E., Kleiner, S.C., Koch, D.G., Patten, B.M., Schieder, R., Snell, R.L., Stauffer, J.R., Tolls, V., Wang, Z., Winnewisser, G., & Zhang, Y.F. 2000, ApJ, **539**, L87.
- Moriarty-Schieven G.H., Hughes V.A., & Snell R.L., 1989, ApJ, **347**, 358.
- Mumma, M.J., Weaver, H.A., & Larson, H.P. 1987, A&A, **187**, 419.
- Neufeld, D.A., Green, J.D., Hollenbach, D.J., Sonnentrucker, P., Melnick, G.J., Bergin, E.A., Snell, R.L., Forrest, W.J., Watson, D.M., Kaufman, M.J. 2006b, ApJ, **647**, L33.
- Neufeld, D.A., Hollenbach, D.J., Kaufman, M.J., Snell, R.L., Melnick, G.J., Bergin, E.A., & Sonnentrucker, P. 2007, ApJ, **664**, 890.
- Neufeld, D.A. & Kaufman, M.J. 1993, ApJ, **418**, 263.
- Neufeld, D.A., & Melnick, G.J. 1991, ApJ, **374**, 784.
- Neufeld, D.A., Melnick, G.J., Sonnentrucker, P., Bergin, E.A., Green, J.D., Kim, K.H., Watson, D.M., Forrest, W.J., & Pipher, J.L. 2006a, ApJ, **649**, 816.

- Neufeld, D.A., Snell, R.L., Ashby, M.L.N., Bergin, E.A., Chin, G., Erickson, N.R., Goldsmith, P.F., Harwit, M., Howe, J.E., Kleiner, S.C., Koch, D.G., Patten, B.M., Plume, R., Schieder, R., Stauffer, J.R., Tolls, V., Wang, Z., Winnewisser, G., Zhang, Y.F., & Melnick, G.J. 2000, *ApJ*, **539**, L107.
- Nisini, B., Benedettini, M., Giannini, T., Codella, C., Lorenzetti, D., Di Giorgio, A.M., & Richer, J.S. 2000, *A&A*, **360**, 297.
- Snell, R.L., *et al.* 2000, *ApJ*, **539**, L101.
- Snell, R.L., Scoville, N.Z., Sanders, D.B., & Erickson, N.R. 1984, *ApJ*, **284**, 176.
- Torrelles J., Gómez J.F., Rodríguez L.F., Curiel, S., Anglada, G., & Ho, P.T.P. 1998, *ApJ*, **505**, 756.
- Walther D.M., Geballe T.R., & Robson E.I. 1991, *ApJ*, **377**, 246.
- Walther D.M., Robson E.I., Aspin C., & Dent W.R.F. 1993, *ApJ*, **418**, 310.
- Zhou, S., Evans, N. J. II, Güsten, R., Mundy, L.G., & Kutner, M.L. 1991, *ApJ*, **372**, 518.

Table 1. Peak Intensity for Each Mapped Transition

Species	Transition	Rest Wavelength μm	Peak Intensity $10^{-6} \text{ erg cm}^{-2} \text{ s}^{-1} \text{ sr}^{-1}$
H ₂ O	$7_{25} - 6_{16}$	29.837	4.39
	$6_{34} - 5_{05}$	30.899	7.08
	$8_{54} - 7_{43}$	30.871	
	$7_{34} - 6_{25}$	34.549	7.08
H ₂	S(0)	28.221	21.10
	S(1)	17.035	189.31
	S(2)	12.279	1721
	S(3)	9.665	1421
	S(4)	8.025	1200
	S(5)	6.909	3300
	S(6)	6.109	1746
	S(7)	5.511	1800
HD	R(3)	28.502	3.37
	R(4)	23.034	6.20
S I	$^3\text{P}_1 - ^3\text{P}_2$	25.249	201.70
Fe II	$a^6\text{D}_{7/2} - a^6\text{D}_{9/2}$	25.988	40.84
Si II	$^2\text{P}_{3/2} - ^2\text{P}_{1/2}$	34.815	55.41

Table 2. Beam-Averaged Line Fluxes for the H₂O Features Toward H₂O Peak 1

H ₂ O Feature μm	Ortho (o)/ Para (p)	Transition	Rest Wavelength μm	Extinction-Corrected Line Flux $\times 10^{-21}$ into 15'' Beam ^a W cm ⁻²
36.21	p	6 ₂₄ – 5 ₁₅	36.212	1.57
35.92	o	6 ₅₂ – 5 ₄₁	35.938	0.70
	p	6 ₅₁ – 5 ₄₂	35.904	
35.67	o	8 ₄₅ – 7 ₃₄	35.669	0.55
35.45	p	5 ₃₃ – 4 ₀₄	35.472	2.43
	o	7 ₄₃ – 6 ₃₄	35.428	
34.55	o	7 ₃₄ – 6 ₂₅	34.549	2.02
33.13	p	7 ₅₃ – 6 ₄₂	33.127	0.64
32.99	o	16 ₁₁₆ – 15 ₀₁₅	33.042	1.42
	p	16 ₀₁₆ – 15 ₁₁₅	33.042	
	o	6 ₆₁ – 5 ₅₀	33.005	
	p	6 ₆₀ – 5 ₅₁	33.005	
	o	7 ₅₂ – 6 ₄₃	32.991	
	o	15 ₁₁₄ – 14 ₂₁₃	32.965	
	p	15 ₂₁₄ – 14 ₁₁₃	32.960	
31.75	o	4 ₄₁ – 3 ₁₂	31.772	0.70
	p	8 ₄₄ – 7 ₃₅	31.738	
30.89	o	6 ₃₄ – 5 ₀₅	30.899	1.82
	o	8 ₅₄ – 7 ₄₃	30.871	
30.53	p	7 ₆₂ – 6 ₅₁	30.529	0.63
	o	7 ₆₁ – 6 ₅₂	30.526	
29.84	o	7 ₂₅ – 6 ₁₆	29.837	1.27

^a At the spectral resolving power of *Spitzer*/IRS, some H₂O features may be blends of two or more H₂O transitions. The line fluxes listed here represent the *total* flux for each H₂O feature.

Table 3. Beam-Averaged Line Fluxes for Key Species Toward H₂O Peak 1

Species	Transition	Rest Wavelength μm	Extinction-Corrected Line Flux $\times 10^{-21}$ into 15'' Beam W cm^{-2}
H ₂	S(7)	5.5112	275.2
H ₂	S(6)	6.1086	110.9
H ₂	S(5)	6.9095	513.0
H ₂	S(4)	8.0251	207.0
H ₂	S(3)	9.6649	474.4
H ₂	S(2)	12.2786	138.1
H ₂	S(1)	17.0348	68.3
HD	R(4)	23.0338	2.2
OH	$^2\Pi_{3/2} 23/2^+ - 21/2^-$	25.0351	0.41
OH	$^2\Pi_{3/2} 23/2^- - 21/2^+$	25.0899	0.48
[S I]	$^3P_1 - ^3P_2$	25.2490	78.8
[Fe II]	$a^6D_{7/2} - a^6D_{9/2}$	25.9883	7.6
OH	$^2\Pi_{3/2} 21/2^- - 19/2^+$	27.3935	0.13
OH	$^2\Pi_{3/2} 21/2^+ - 19/2^-$	27.4546	0.58
OH	$^2\Pi_{1/2} 19/2^- - 17/2^+$	27.6516	0.31
OH	$^2\Pi_{1/2} 19/2^+ - 17/2^-$	27.6967	0.26
H ₂	S(0)	28.2188	9.1
HD	R(3)	28.5020	2.3
OH	$^2\Pi_{3/2} 19/2^+ - 17/2^-$	30.2772	0.25
OH	$^2\Pi_{3/2} 19/2^- - 17/2^+$	30.3459	0.60
OH	$^2\Pi_{1/2} 17/2^+ - 15/2^-$	30.6573	0.33
OH	$^2\Pi_{1/2} 17/2^- - 15/2^+$	30.7063	0.37
[S III]	$^3P_1 - ^3P_0$	33.4800	1.5
[Si II]	$^2P_{3/2} - ^2P_{1/2}$	34.8152	18.7

Table 4. Best-Fit Physical Conditions Within H₂O Peak 1 Inferred from H₂ S(0)-S(1) Lines

Parameter	Log ₁₀ H ₂ Density (cm ⁻³)						
	4.0	4.5	5.0	5.5	6.0	6.5	7.0
Warm Component:							
Temperature (K)	377	361	352	344	336	330	328
Log ₁₀ N(H ₂) (cm ⁻²) – measured . . .	20.60	20.61	20.61	20.60	20.59	20.59	20.58
Log ₁₀ N(H ₂) (cm ⁻²) – theory	20.54	20.81	21.06	21.32	21.57	21.83	22.08
H ₂ Ortho-to-Para Ratio	0.69	0.71	0.68	0.63	0.58	0.55	0.53
Beam Filling Factor	1.0	0.64	0.35	0.19	0.10	0.06	0.03
Mass of Warm H ₂ (× 0.1 M _⊙)	0.04	0.07	0.12	0.21	0.38	0.68	1.22
Hot Component:							
Temperature (K)	2111	1621	1341	1169	1070	1024	1006
Log ₁₀ N(H ₂) (cm ⁻²) – measured . . .	19.31	19.38	19.47	19.58	19.66	19.71	19.73
Log ₁₀ N(H ₂) (cm ⁻²) – theory	20.13	20.44	20.74	21.02	21.29	21.55	21.81
H ₂ Ortho-to-Para Ratio ^a	3.45	3.58	3.68	3.68	3.62	3.56	3.53
Beam Filling Factor	0.15	0.09	0.05	0.04	0.02	0.01	0.008
Mass of Hot H ₂ (× 0.1 M _⊙)	0.01	0.03	0.06	0.11	0.20	0.36	0.65

^a Errors on the H₂ ortho-to-para ratio are hard to estimate, but the best-fit values for the hot component are probably consistent with the LTE value of 3.

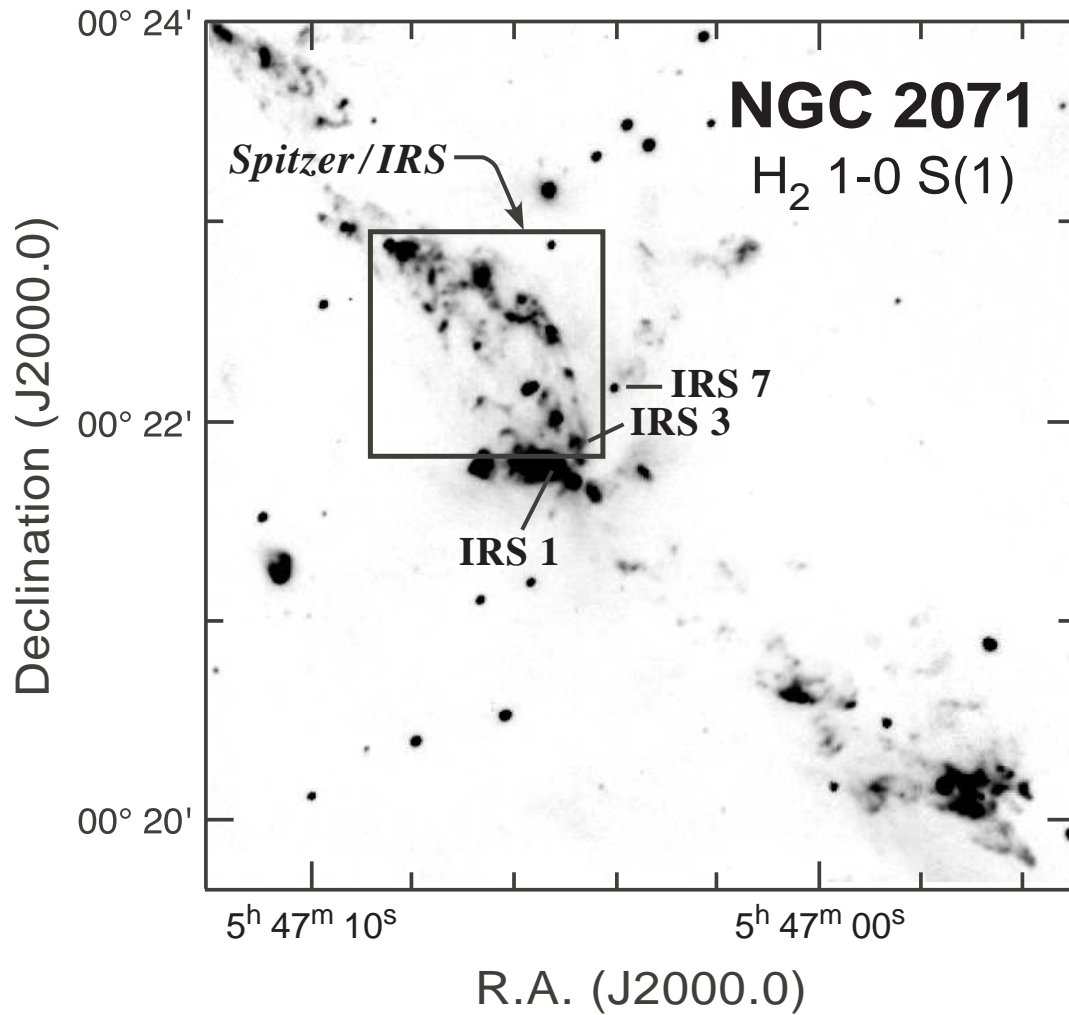


Fig. 1. Map of the northern lobe of the outflow from NGC 2071 as traced by the H₂ 1-0 S(1) 2.12 μ m emission (after Eislöffel 2000). The driving source of the NGC 2071 outflow is believed centered close to RA 05^h 47^m 04^s.6, Dec +00° 21' 48" (J2000). The box labeled *Spitzer/IRS* bounds the portion of the northern outflow lobe observed here.

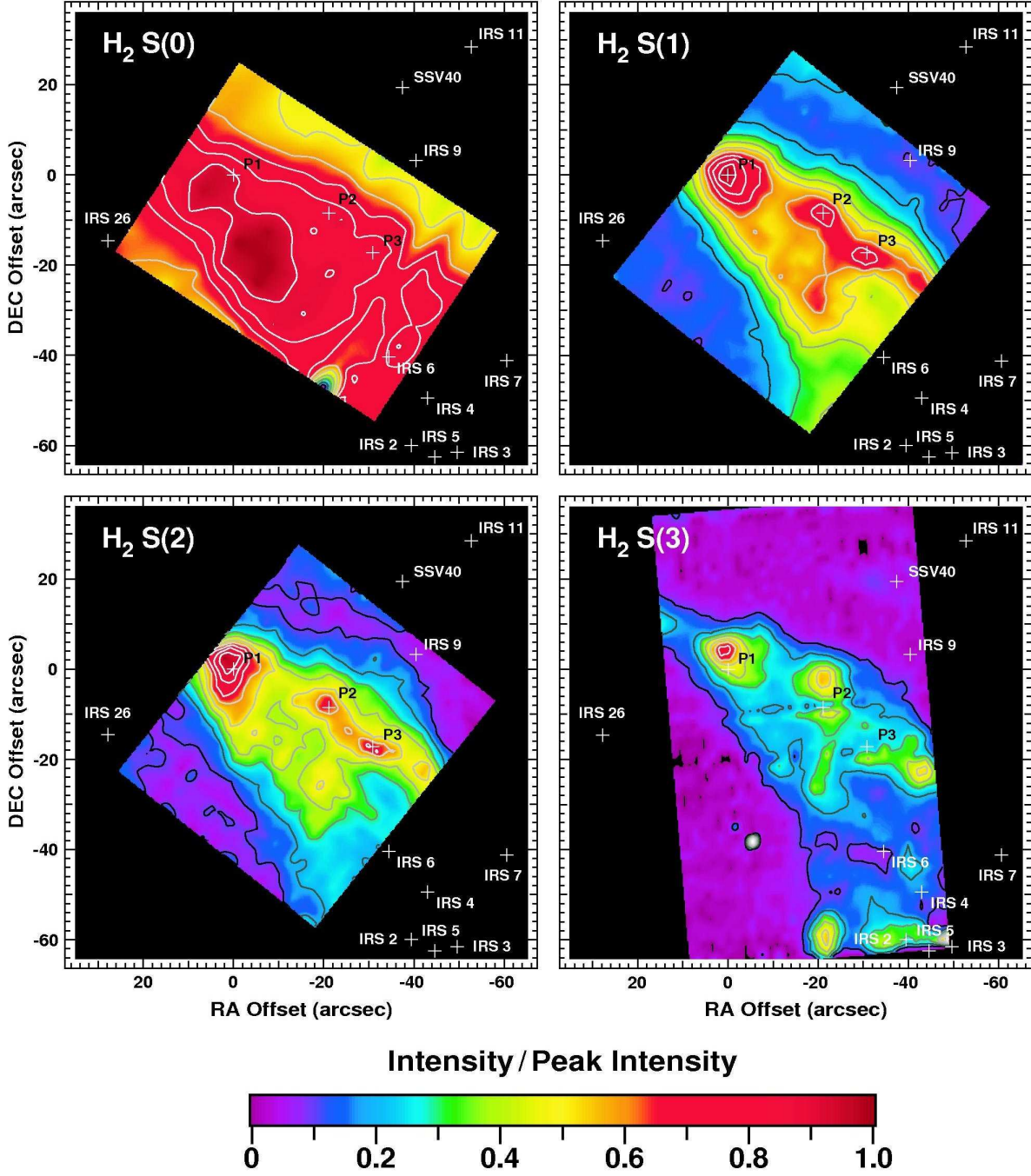


Fig. 2. Map of the northern lobe of the outflow from NGC 2071 as traced by H_2 S(0) through S(3) emission. Offsets are relative to the measured peak of the H_2 $17.035 \mu\text{m}$ S(1) emission centered at RA $05^{\text{h}} 47^{\text{m}} 08^{\text{s}}.1$, Dec $+00^{\circ} 22' 50.7''$ (J2000). The peak intensity for each transition is provided in Table 1. Positions P1, P2, and P3 are fiducials that mark the positions of the first, second, and third strongest peaks in the H_2 S(1) emission. The position of other known sources in the field are also shown (cf. Walther *et al.* 1993).

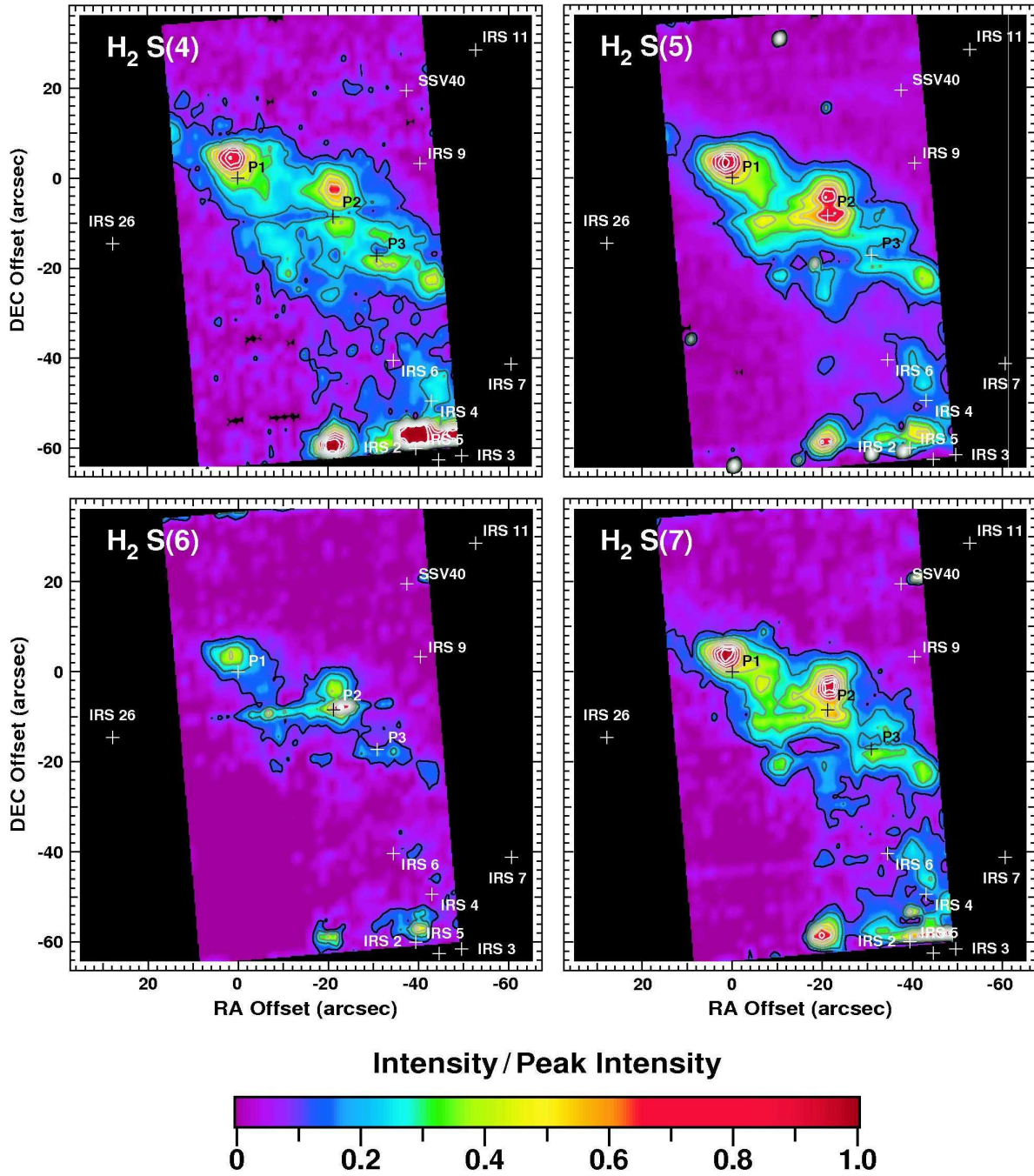


Fig. 3. Same as Fig. 2, except for H₂ S(4) through S(7) emission.

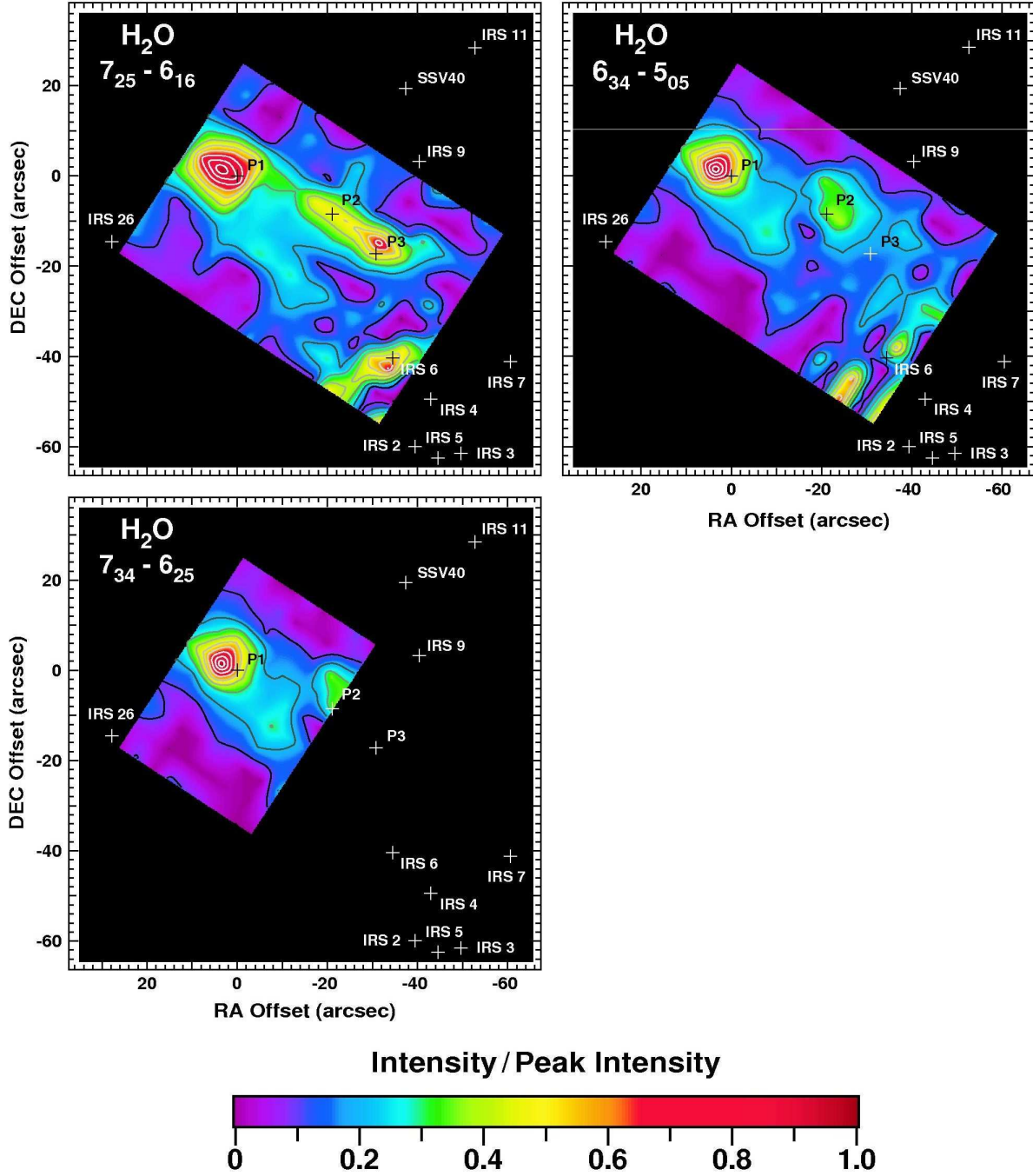


Fig. 4. Same as Fig. 2, except for H₂O $7_{25}-6_{16}$ 29.837 μm , $6_{34}-5_{05}$ 30.899 μm (blended with H₂O $8_{54}-7_{43}$ 30.871 μm), and $7_{34}-6_{25}$ 34.549 μm emission. The H₂O $7_{34}-6_{25}$ map is truncated because *Spitzer*/IRS was exposed to a strong source while slewing to the NGC 2071 field. This caused latent signal levels at the long wavelength end of LH and, thus, we conservatively omitted these less reliable observations.

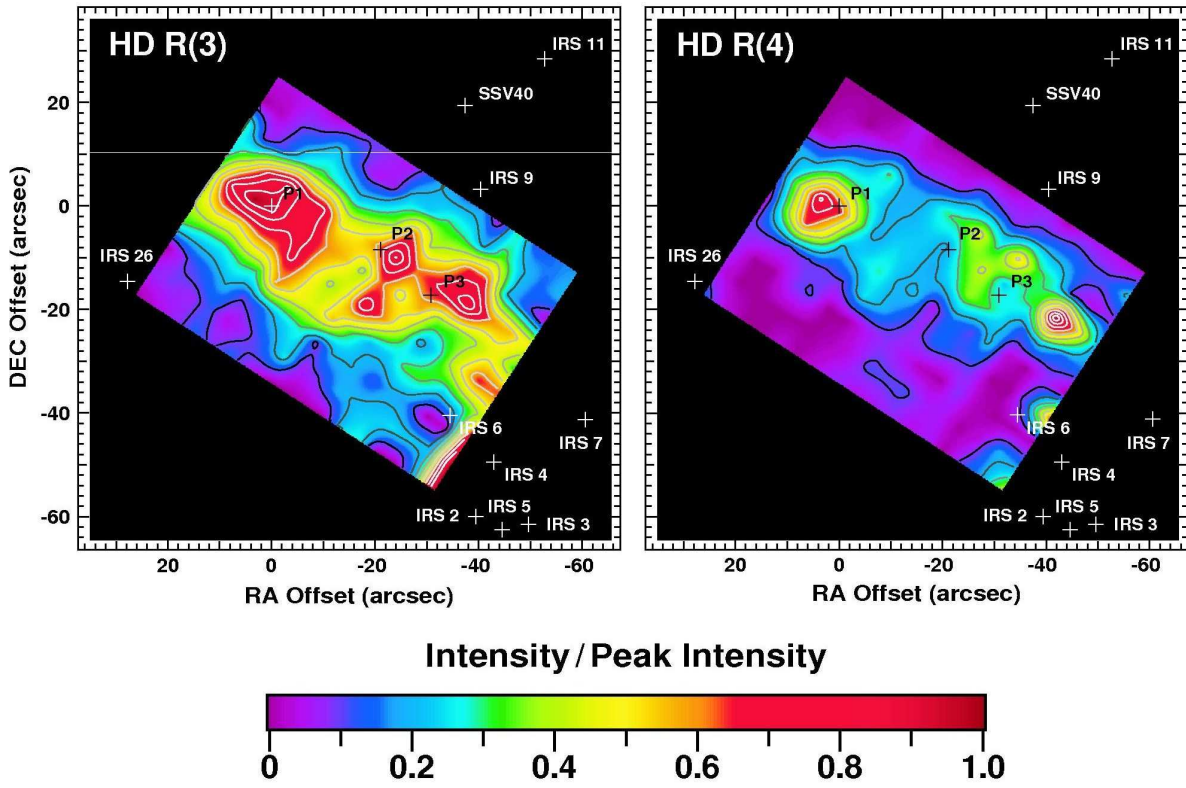


Fig. 5. Same as Fig. 2, except for HD R(3) $28.502 \mu\text{m}$ and R(4) $23.034 \mu\text{m}$ pure rotational emission.

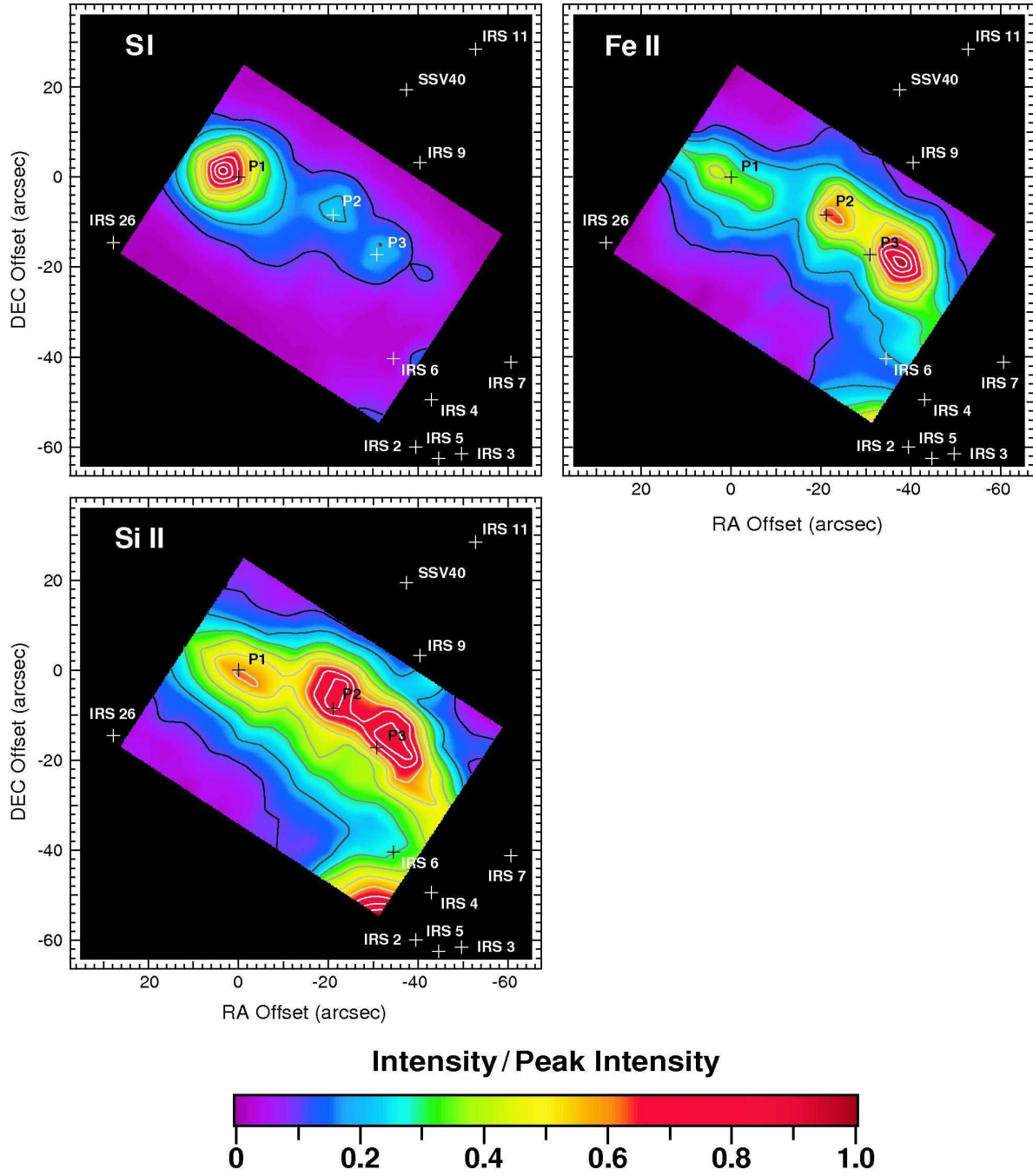


Fig. 6. Same as Fig. 2, except for Si I $^3P_1 - ^3P_2$ 25.249 μm , Fe II $a^6D_{7/2} - a^6D_{9/2}$ 25.988 μm , and Si II $^2P_{3/2} - ^2P_{1/2}$ 34.815 μm emission.

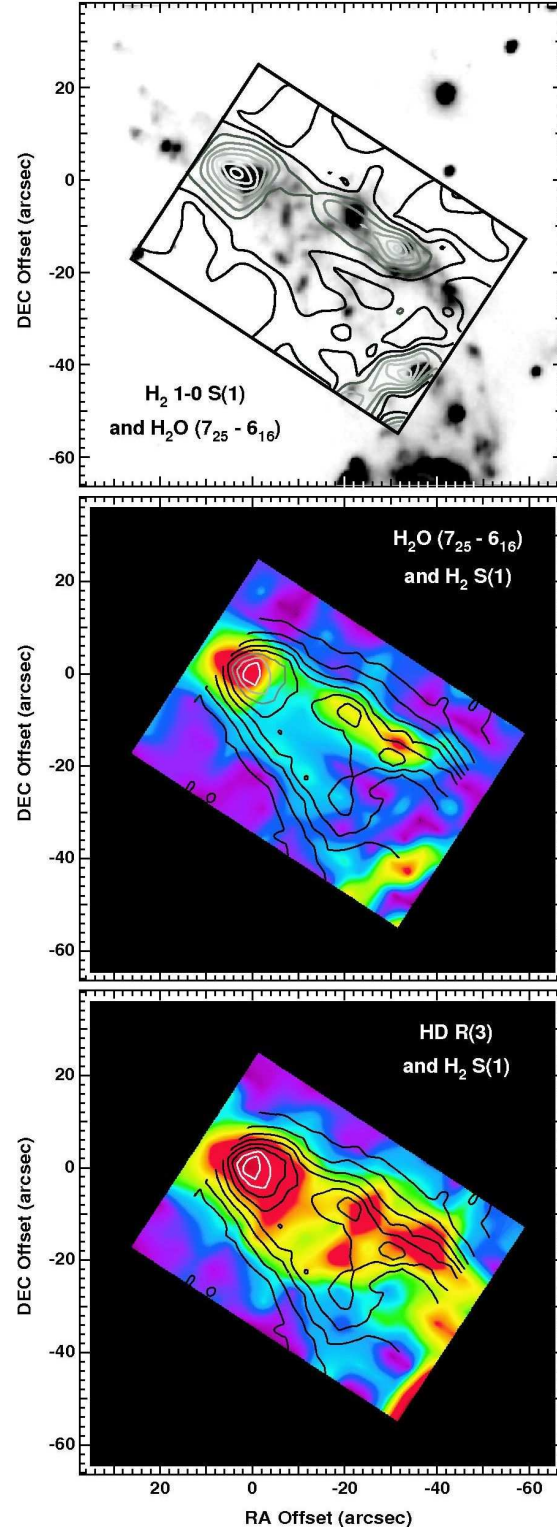


Fig. 7. *Top:* Contours of H_2O $7_{25}-6_{16}$ $29.837\ \mu\text{m}$ emission superposed on the Eisloffel (2000) H_2 1-0 S(1) $2.12\ \mu\text{m}$ map. *Middle:* Contours of H_2 S(1) emission superposed on the map of H_2O $7_{25}-6_{16}$ $29.837\ \mu\text{m}$ emission. *Bottom:* Contours of H_2 S(1) emission superposed on the map of HD R(3) $28.502\ \mu\text{m}$ emission

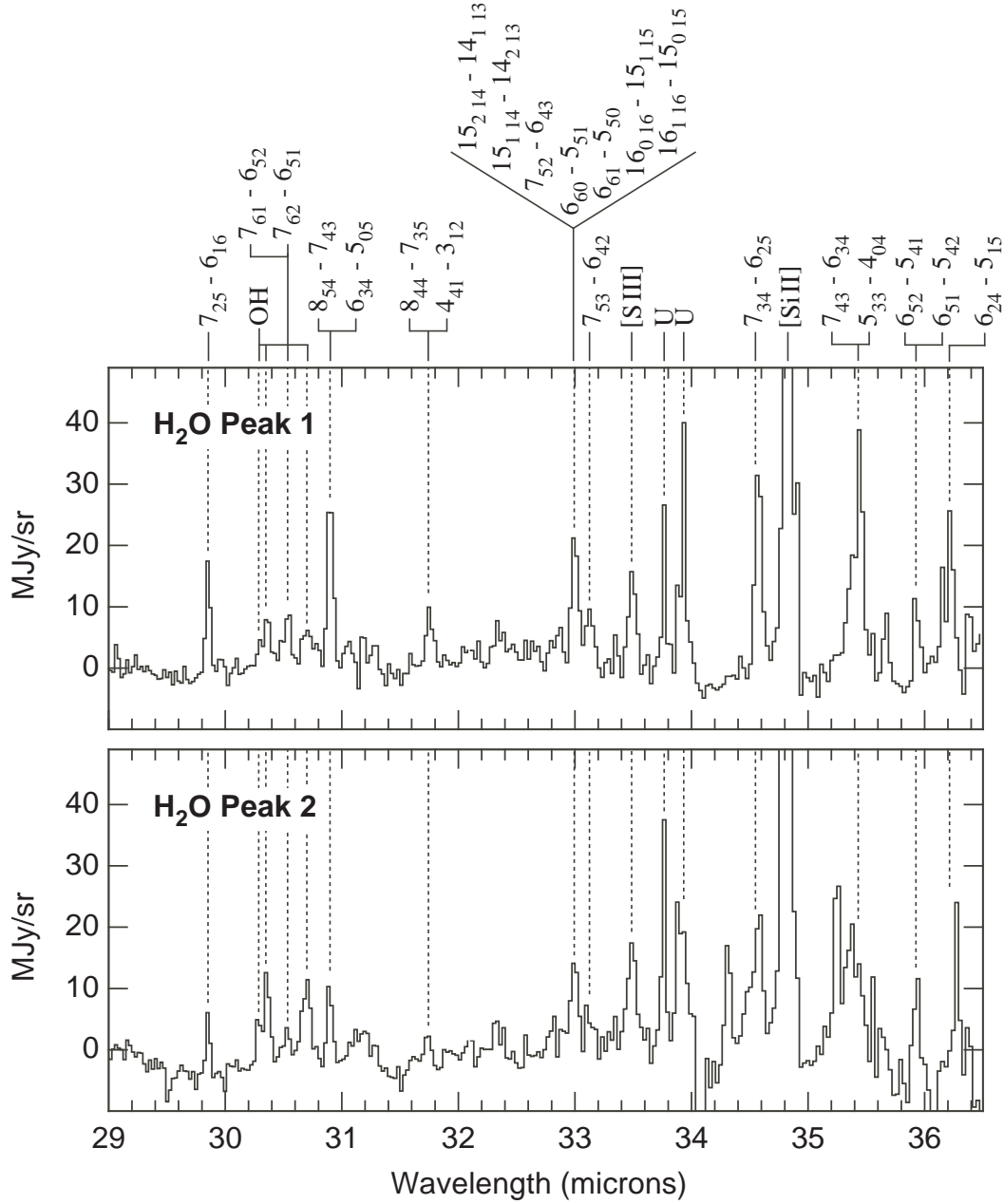


Fig. 8. Portion of the *Spitzer/IRS* spectra obtained in a 15'' synthesized beam toward H₂O Peaks 1 and 2 (see text). The H₂¹⁶O transition(s) associated with each detected feature are shown. In the absence of higher spectral resolving power, we are not able to observationally determine the extent to which each transition contributes to the total flux measured for each blended feature. In addition to Si II and S III lines in the band, we also note the tentative detection of OH ²Π_{3/2} 19/2⁺-17/2⁻ 30.277 μm, ²Π_{3/2} 19/2⁻-17/2⁺ 30.346 μm, ²Π_{1/2} 17/2⁺-15/2⁻ 30.657 μm. Unidentified lines are denoted with a “U”.

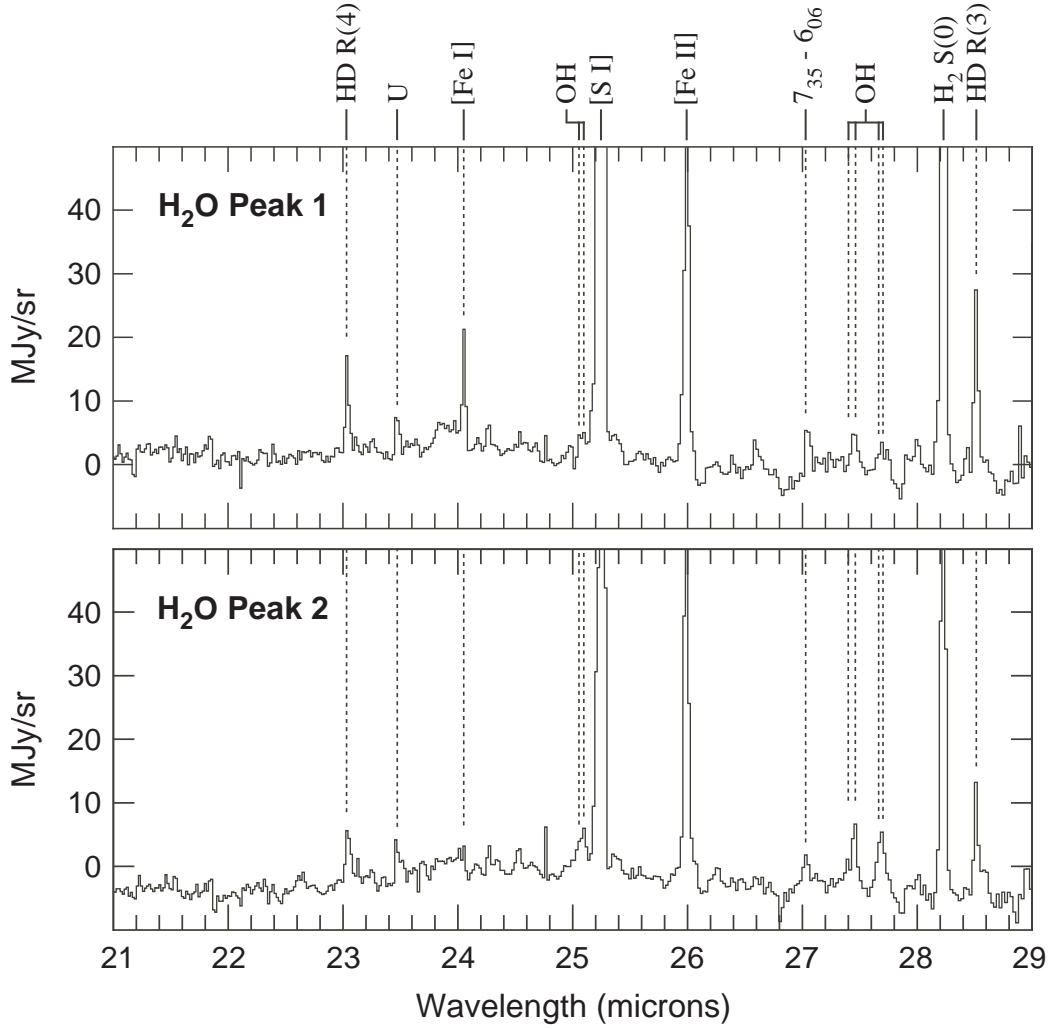


Fig. 9. Portion of the *Spitzer/IRS* spectra obtained in a $15''$ synthesized beam toward H₂O Peaks 1 and 2 (see text). Of particular note is the ground rotational transition of para-H₂ at $28.219\ \mu\text{m}$, two HD rotational transitions, R(3) and R(4), at 28.502 and $23.034\ \mu\text{m}$, respectively, and the tentative detection of OH $^2\Pi_{3/2}\ 21/2^- - 19/2^+$ $27.393\ \mu\text{m}$, $^2\Pi_{3/2}\ 21/2^+ - 19/2^-$ $27.454\ \mu\text{m}$, $^2\Pi_{1/2}\ 19/2^- - 17/2^+$ $27.652\ \mu\text{m}$, $^2\Pi_{1/2}\ 19/2^+ - 17/2^-$ $27.697\ \mu\text{m}$, $^2\Pi_{3/2}\ 23/2^+ - 21/2^-$ $25.035\ \mu\text{m}$, and $^2\Pi_{3/2}\ 23/2^- - 21/2^+$ $25.090\ \mu\text{m}$. Unidentified lines are denoted with a “U”.

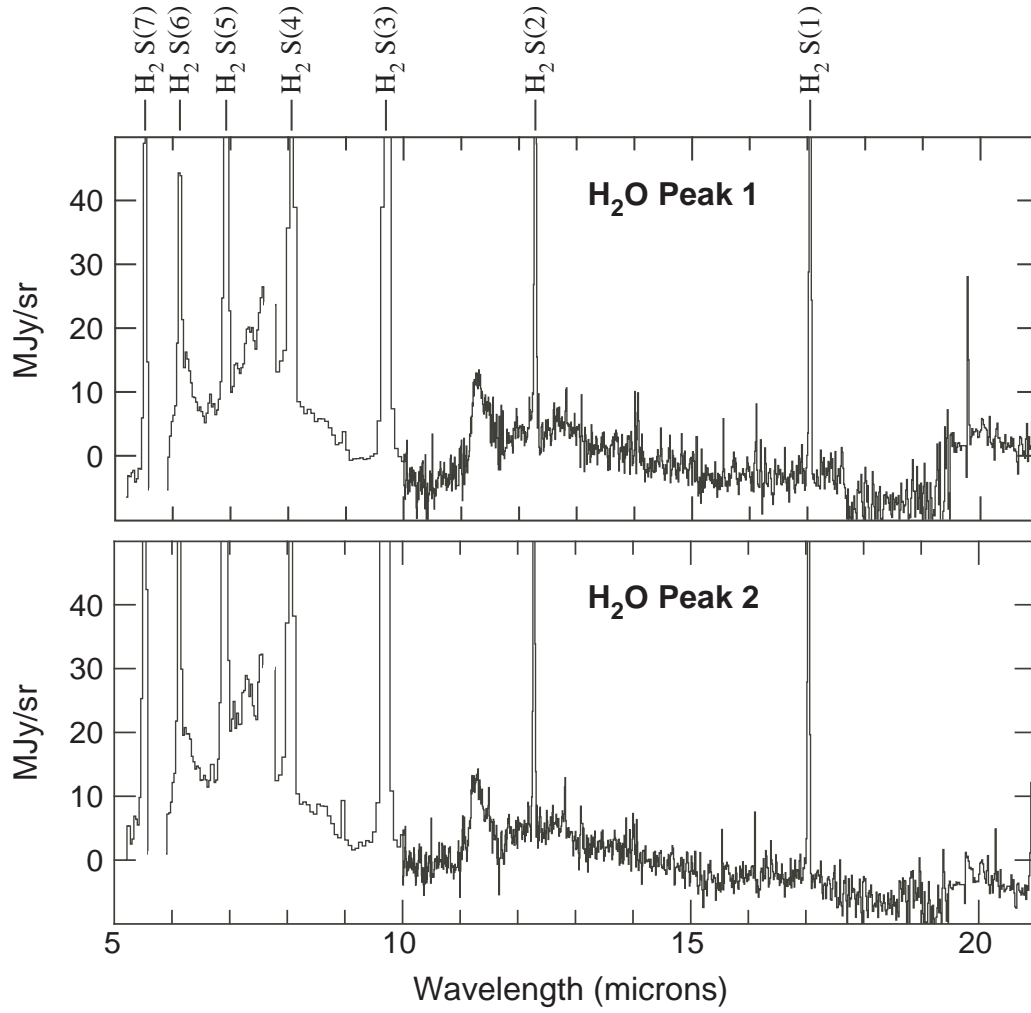


Fig. 10. Portion of the *Spitzer/IRS* spectra obtained in a 15'' synthesized beam toward H₂O Peaks 1 and 2 (see text). Of note are the prominent lines of H₂S(1) through (7). Both spectra also show broad PAH emission features with peak wavelengths of 6.22, 7.41, 7.59, 7.85, 8.61, and 11.3 μm .

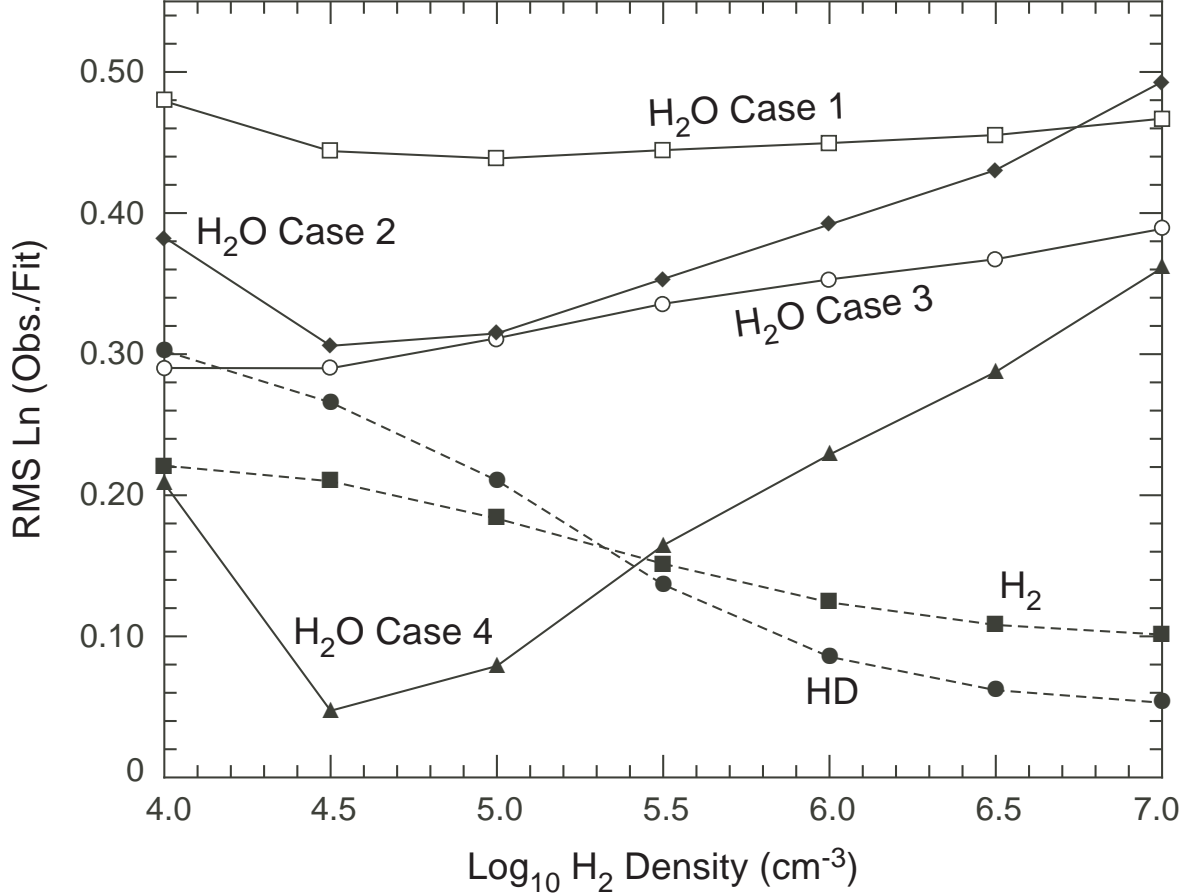


Fig. 11. Root mean square goodness-of-fit of the computed fluxes at each density for H₂ S(0) – S(7) (*dashed line-solid squares*); HD R(3) and R(4) (*dashed line-solid circles*); H₂O Case 1 – the H₂O features listed in Table 2, with the exception of the 34.55 μ m feature, and assuming an ortho-to-para ratio of 3:1 (*open squares*); H₂O Case 2 – the pure ortho- or para-H₂O lines at 29.84, 33.13, and 36.21 μ m and assuming an ortho-to-para ratio of 3:1 (*solid diamonds*); H₂O Case 3 – the H₂O features listed in Table 2, with the exception of the 34.55 μ m feature, and assuming an ortho-to-para ratio that has been allowed to vary to produce the best fit to the data at each density (*open circle*); H₂O Case 4 – the pure ortho- or para-H₂O lines at 29.84, 33.13, and 36.21 μ m and assuming an ortho-to-para ratio that has been allowed to vary to produce the best fit to the data at each density (*solid triangles*).

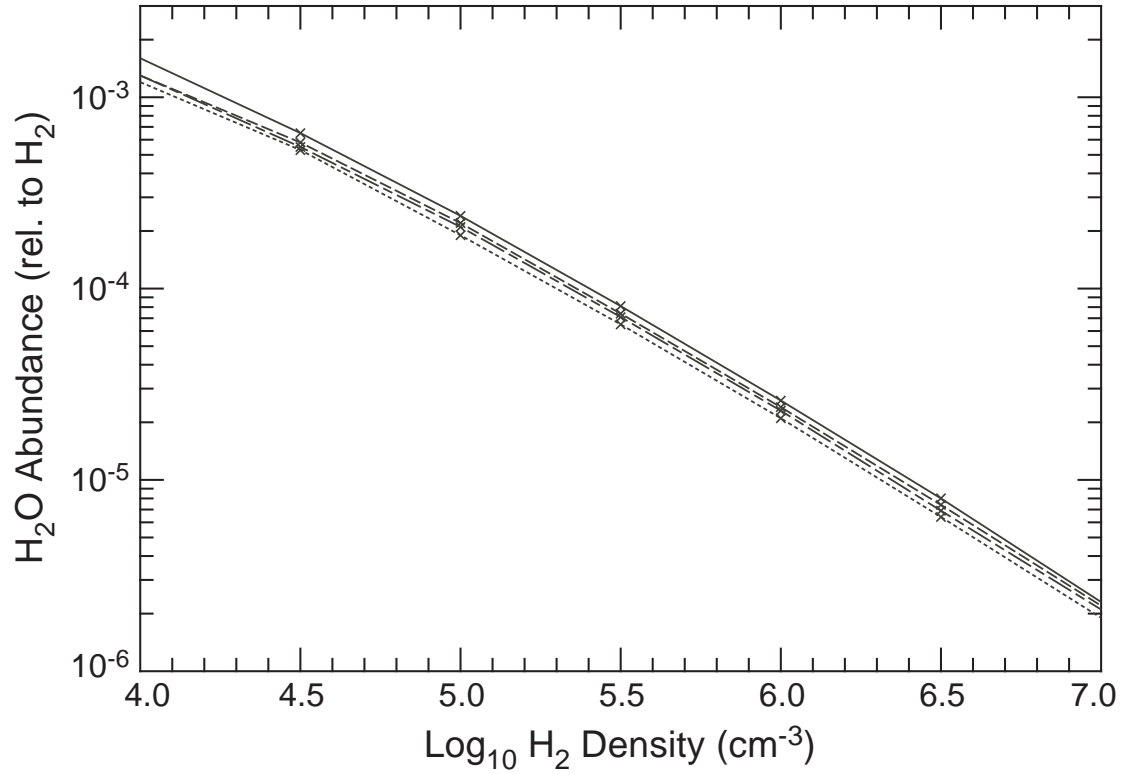


Fig. 12. Total (ortho+para) water abundance, at each assumed density, that produces the best overall fit to: (1) the H₂O features listed in Table 2, with the exception of the 34.55 μm feature, and assuming an ortho-to-para ratio of 3:1 (*dashed line*); (2) the H₂O features listed in Table 2, with the exception of the 34.55 μm feature, and assuming an ortho-to-para ratio that has been allowed to vary to produce the best fit to the data at each density (*dot-dashed line*); (3) the 29.84, 33.13, and 36.21 μm features and assuming an ortho-to-para ratio of 3:1 (*solid line*); and, (4) the 29.84, 33.13, and 36.21 μm features and assuming an ortho-to-para ratio that has been allowed to vary to produce the best fit to the data at each density (*dotted line*).

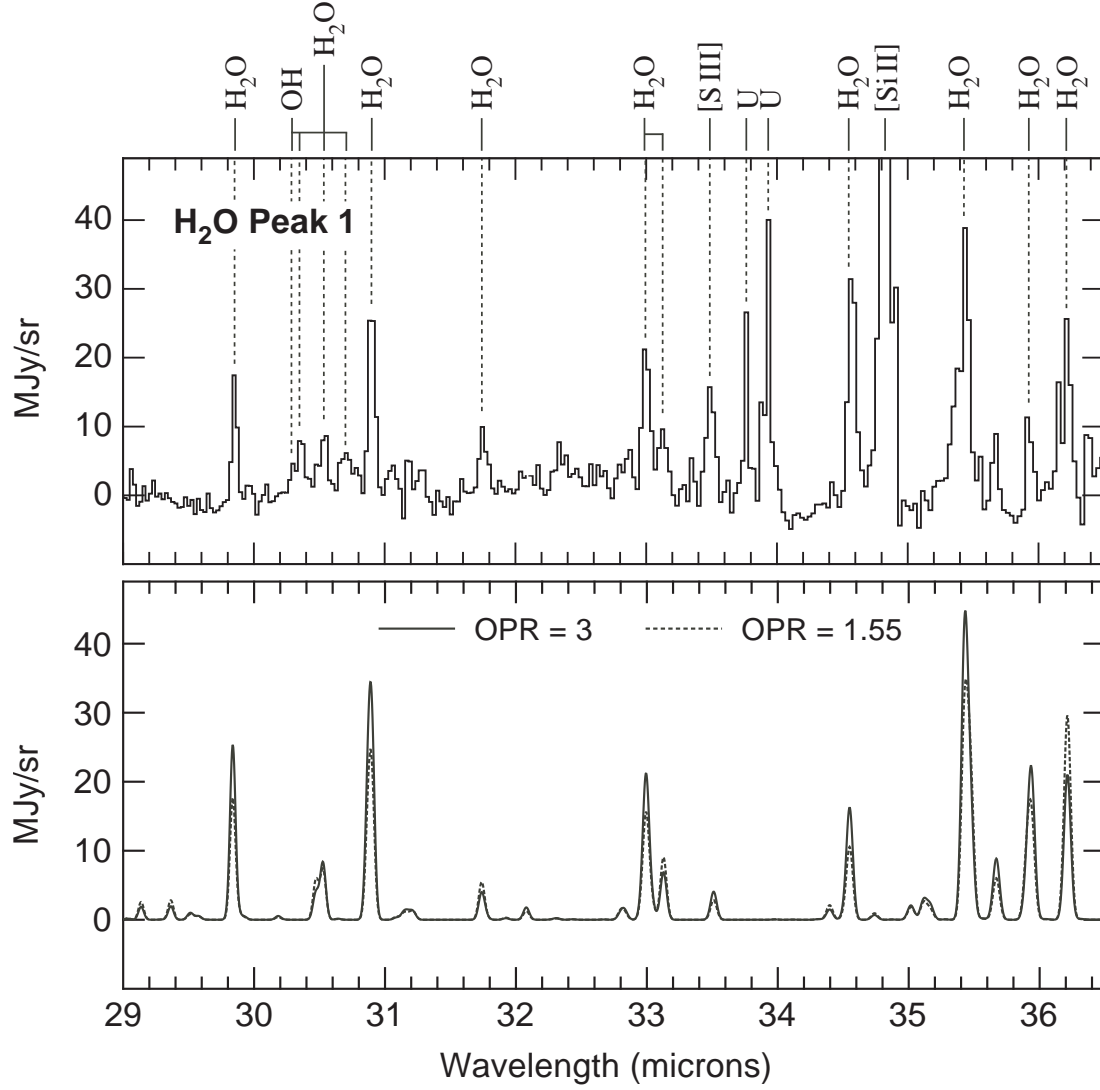


Fig. 13. *Top:* Observed spectrum within 15'' synthesized beam toward H₂O Peak 1. *Bottom:* Model spectra assuming $n(\text{H}_2) = 10^5 \text{ cm}^{-3}$ and an H₂O ortho-to-para ratio of 3:1 (*solid line*) and an H₂O ortho-to-para of 1.55:1 (*dotted line*), which provides the best fit to the pure ortho 29.84 μm and pure para 33.13 and 36.21 μm lines at this density.

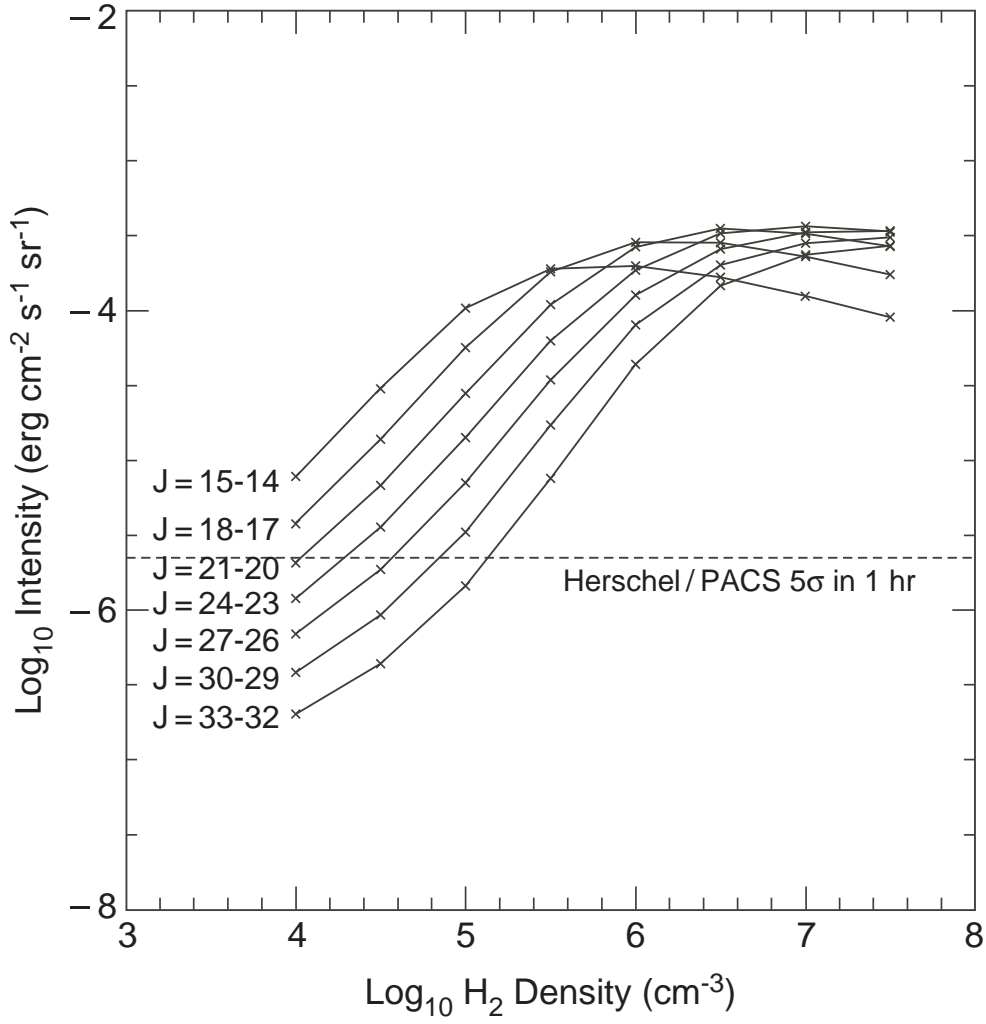


Fig. 14. Computed ^{12}CO line intensities expected for a CO abundance of 10^{-4} relative to H_2 (see text). The dashed line corresponds to the *Herschel*/PACS spectral line sensitivity of $\sim 2 \times 10^{-6} \text{ erg cm}^{-2} \text{ s}^{-1} \text{ sr}^{-1}$ (5σ in 1 hour, corresponding to a flux of $5 \times 10^{-18} \text{ W m}^{-2}$ into a $9.7 \times 9.7''$ pixel).

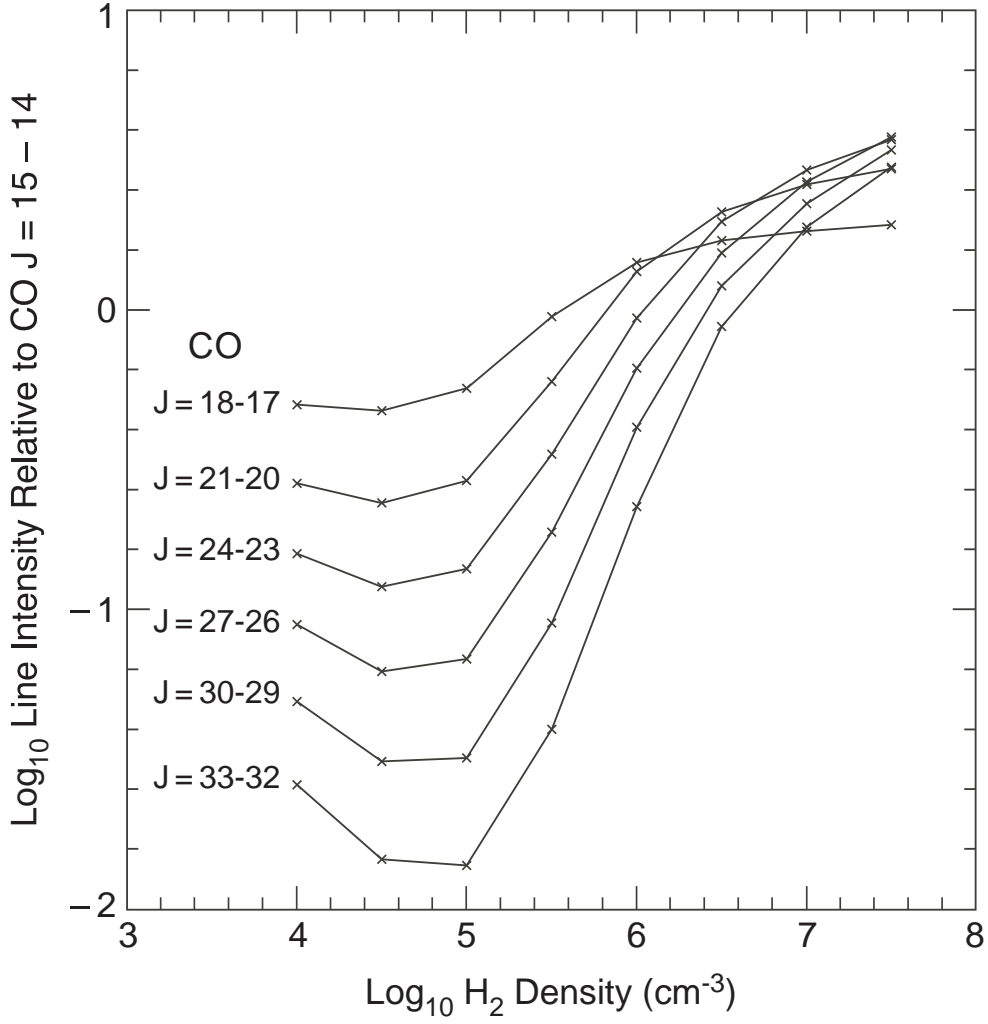


Fig. 15. Computed line intensity ratios of select ^{12}CO high- J rotational transitions with respect to the $^{12}\text{CO } J = 15-14$ line measurable with the *Herschel Space Observatory*. These line ratios are particularly sensitive to H_2 densities between 10^5 and about $3 \times 10^6 \text{ cm}^{-3}$.